

Article

From CT Scans to Morphable Digital Models: Methodologies for Revealing and Preserving the Internal Structures of Artistic Figurines

Christina Sakellariou ¹, Dimitrios Makris ^{1,*}  and Georgios Bardis ²

¹ Department of Conservation of Antiquities and Works of Art, University of West Attica, 12243 Egaleo, Greece; csakellariou@uniwa.gr

² Advanced Knowledge, Image & Information Systems Research Lab, Department of Informatics and Computer Engineering, University of West Attica, Egaleo Park Campus, 12243 Athens, Greece; gbardis@uniwa.gr

* Correspondence: demak@uniwa.gr

Abstract: The revelation of the internal structure of objects through computed tomography (CT scan) contributes to a more comprehensive understanding of their creation, the assessment of their preservation status, and the prediction of their future behavior. Consequently, in the case of Yiannis Pappas' collection, this knowledge aids in the perpetuation of the models it hosts, which are made from malleable materials, such as wax, plasticine, and mazut, on metallic armature. This publication presents the complete methodology for extracting three-dimensional (3D) models (reconstructions) of the individual construction materials of the figurines, with the aim of subsequently utilizing them in research, as well as in their digital preservation and restoration. The 3D reconstructions were obtained by automatic segmentation algorithms based on the absorption measurements of the materials of the specific figurines, and were further edited (post-processing) to obtain the final models.

Keywords: CT scan; hounsfield value; 3D reconstruction; figurine; wax; mazut; plasticine; armature; WebGL; intelligent graphics



Citation: Sakellariou, C.; Makris, D.; Bardis, G. From CT Scans to Morphable Digital Models: Methodologies for Revealing and Preserving the Internal Structures of Artistic Figurines. *Heritage* **2024**, *7*, 5641–5659. <https://doi.org/10.3390/heritage7100266>

Academic Editor: Geert Verhoeven

Received: 14 July 2024

Revised: 17 September 2024

Accepted: 30 September 2024

Published: 9 October 2024



Copyright: © 2024 by the authors. Licensee MDPI, Basel, Switzerland. This article is an open access article distributed under the terms and conditions of the Creative Commons Attribution (CC BY) license (<https://creativecommons.org/licenses/by/4.0/>).

1. Introduction

The creative journey of the significant 20th-century Greek artist, Yannis Pappas, is reflected in the numerous artworks housed in his studio [1]. In these artworks, one can study the process from conception to final creation, the multitude of tests and transformations to the approach of his inner vision, as well as the evolution of his technique over time. The collection includes numerous figurines made from malleable materials such as wax, plasticine, and mazut, shaped over a metal armature, which exhibit a notable pathology. In addition to common issues such as losses, cracks, and material degradation, the figurines display plastic deformations and instability. The current preservation state of ten figurines was initially recorded using structure-from-motion (SfM) photogrammetry with the aim of their preservation, study, and digital restoration [2].

Artists have long used armatures as internal support structures to provide stability and shape to their sculptures [3]. Knowledge of a figurine's internal structure is crucial not only for its physical preservation but also for understanding the artist's technique and the historical context of its creation. The discovery of the complex wire armature inside Edgar Degas' *Little Dancer*, revealed through X-ray examination, exemplifies the importance of understanding an artwork's internal framework [4].

This article focuses on the examination of the figurines' armature through computed tomography (CT scan) with the view to the creation of digital twins, suitable for digital restoration as well as stability examination and the simulation of their future behavior, with finite elements analysis, and past behavior, through known state(s) morphing interpolation. The examination not only revealed their internal structure but also allowed the isolation

and modeling of their individual construction materials, adding to the existing knowledge of materials' HU absorption. The brief description of the figurines is followed by the presentation of the CT scan's findings, the methodology for the extraction of three-dimensional (3D) models using automated segmentation, and, in one of the cases, their utilization to reverse their creative transformation by the artist.

2. Related Works

Computed tomography offers a valuable insight into the internal structure of cultural artifacts through successive scans (two-dimensional imaging) and three-dimensional imaging of the object's entire volume. The imaging capabilities of computed tomography have been applied in the cultural sector from an early stage. Just a few years after the first CT scanner became operational in 1971, the first mummy was scanned in Canada [5]. Since then, a wide range of human and animal remains have been examined [6–13], to draw conclusions about their anatomy and pathology [14–16], dietary habits [17,18], burial practices and customs such as the mummification process [19,20], the construction or reuse of sarcophagi [21,22], and burial offers [23,24]. CT scan data have even been used for facial reconstruction [25].

Medical CT scanners are specifically designed and calibrated for the examination of humans [26,27]. Since cultural artifacts consist of diverse materials, vary in size, and present difficulties in transportation and re-examination, many educational and cultural institutions and organizations were prompted to develop their own systems, such as micro-CT scanners with voxel sizes of a few microns [26,28–30]. Regardless of the system deployed, CT scanning of cultural artifacts yields valuable insights for a thorough understanding of the artifact and, so far, wooden, ceramic, stone, plaster, glass objects, excavation finds, frescoes, and even basketry have been scanned [30–32].

The acquisition of data regarding the spatial distribution of the construction material(s) within the object contributes to the understanding of its structure and construction method [26,33]. The visualization of internal supporting structures, as armatures [26,34,35], the connectivity of the various structural elements and materials [27], and the morphology of the internal surfaces [36–38] is headed in the aforementioned direction. In some cases, CT scan reveals the presence of objects [39–42] or even human remains [43]. The results of CT scanning can also address research questions concerning inaccessible or hidden areas of objects [5,31,44,45], assist in the authentication of artifacts [46–48], provide relative dating [35], or even be deployed in strength tests of structural elements [49].

The visualization of the interior of the artifacts contributes to a more comprehensive documentation of their preservation status and pathology, as it aids in the identification and estimation of the size of the damage, as in cases of cracks [26] and wood infestation [26,49]. Information regarding the material's grain size, possible discontinuities, or voids could lead to conclusions about the loss of substrate cohesion [32]. The density, volume, and weight of internal structures can be calculated [26,37,48], differences in material density can be detected [50], and the thickness of layers measured [47]. In some cases, it has revealed the use of different types of materials such as wood [26], glass [51], and gypsum [18], and specifically in wooden structures, wood species identification and dendrochronology may be feasible [52–55]. The different HU absorption values of the materials has also contributed in the identification and mapping of earlier treatments [26,56] and in the evaluation of the course of modern conservation interventions such as impregnation [57,58]. The spatial analysis and classification of construction materials are complemented by detailed material characterization techniques such as XRD, XRF, EDX, and FTIR [32,56].

The processing of the primary data can lead to the creation of 3D models and prints of the examined item, which facilitate its further study. Three-dimensional imaging of the interior of objects or excavated blocks of soil containing fragile findings assist their safe extraction [28,59–61] or virtual examination. During CT's data 3D reconstruction, specific absorption areas can be isolated, studied, and modeled, such as human or animal skeletons [11,26,34] or the contents of burial sites [21,61,62]. Indicatively, the reconstruction

and 3D printing of an amulet found inside a wrapped mummy [24] and the gradual unwrapping of the bandages of a mummy [9] have been mentioned in the literature. Special interest lies in the virtual isolation and study of archeological coins from the interior of a ceramic vessel [40]. Finally, the capabilities of computed tomography can be combined with photogrammetry to digitize difficult materials such as translucent glass sculptures [63].

Regarding the creation and printing of 3D organs as part of preoperative assessment, personalized implants, and prosthetics, research is now commonplace in the medical community. Commercial software, particularly Materialize Mimics (developed by Materialise, Belgium) [64,65], predominates in this field. Notable options among freely available software are Seg3D (developed by the SCI Institute, University of Utah, USA), 3D Slicer (Harvard Medical School, USA, available at www.slicer.org), InVesalius (developed by the Renato Archer Information Technology Center, Brazil), ITK-SNAP (a joint effort by the University of Pennsylvania and University of Utah, available at www.itksnap.org), and Horos for MacOS environments (available at <https://horosproject.org>) [11,66–69]. Initially, three-dimensional models are imported into processing software such as MeshLab (available at <https://meshlab.net>), Blender (available at <https://blender.org>), Maya (Autodesk), and ZBrush (Pixologic) [67,70], and the final model was either printed [66,71] or used in AR or VR applications [70]. The general workflow comprises three steps: image segmentation, mesh optimization, and 3D printing [64,66,67,70–73]. The process of converting CT scans into 3D models begins with overlaying the scans taken at intervals of the defined step. During this process, pixel intensities are interpolated between adjacent scans, forming voxel data. The 3D modeling process involves the definition of discrete parts that represent the desired structure (segmentation) [66,70,74]. Image segmentation algorithms are based on intensity, discontinuity, and similarity or segmentation techniques [66,70], with the most common techniques including thresholding, edge detection, region growing [70,73,75], and currently machine learning techniques, such as Convolutional Neural Networks (CNN) [64,74,76]. The final result is affected by various scanning parameters, such as the scan step, the adjustment of contrast and brightness, artifacts like noise, streaks, distortions, as well as the parameters for exporting the.stl file format, such as the number of triangles and automatic smoothing [64,73,75].

3. Materials and Methods

3.1. Description

The following five figurines are part of a broader study on the possible methods of digital restoration and reconstruction of artifacts made of malleable materials (Figure 1).

The Xenophanes figurine (EPG_972) exhibits plastic deformations and stability issues. The philosopher now leans forward and turns to the right. His head is detached, and his arms have suffered significant material loss. It is made of wax, with localized additions of plasticine, which has become brittle and developed an extensive network of micro-cracks.

The seated elderly figure (EPG_102) is also made of wax, with localized use of plasticine. In addition to the severe lean of the torso and head, and the detached hand, his right leg is held in place only due to its internal skeleton, but it has twisted and shifted outward, risking breakage.

In the small equestrian Alexander (EPG_XA), made of mazut, the horse's hind legs have shifted, causing the entire figure to tilt dangerously to the right. The figurine also has detached parts (foot, leg, and horse tail) and the material appears locally glossy and semi-fluid.

The large equestrian Alexander (EPG_672) is made of plasticine. In this figurine the plasticine has degraded, exhibiting a brownish semi-fluidity (weeping), likely in areas where there is an underlying metallic element. During its conservation, the detached parts were reattached using stainless steel pins.


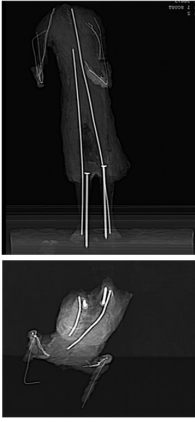
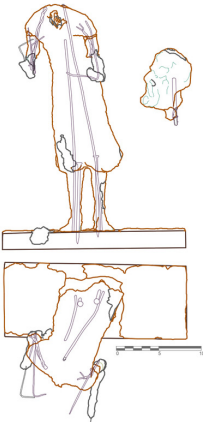


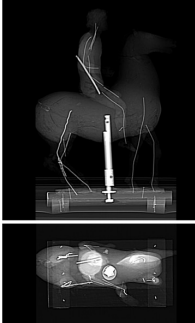
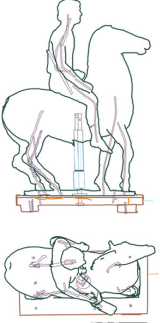


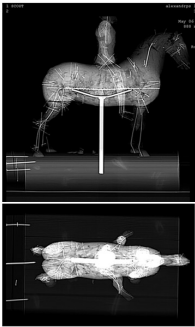
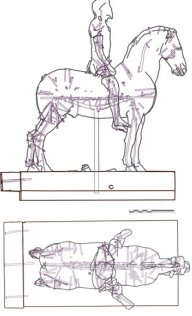
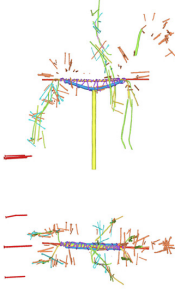

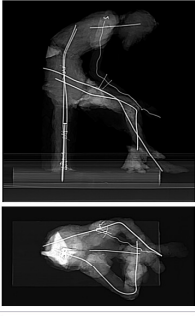
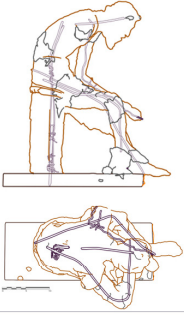
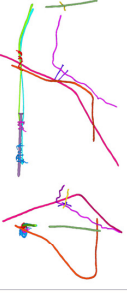

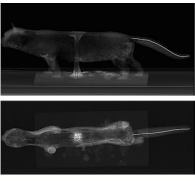
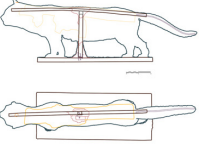

Name/ image	CT scout image	Mapping	3D model of armature (painted)
<p>EGP_972</p> <p>38.3 × 25.2 × 17.8 cm</p> 			
<p>EGP_XA</p> <p>16 × 23 × 30 cm</p> 			
<p>EGP_672</p> <p>40 × 19.5 × 39.5 cm</p> 			
<p>EGP_102</p> <p>38 × 16 × 26 cm</p> 			
<p>EGP_197</p> <p>28 × 20 × 84 cm</p> 			

Figure 1. The five selected figurines (photogrammetry-generated 3D models) along with their scout files (CT scan), mapping, and 3D reconstruction models of the armature.

Finally, the cat model (EPG_197), made of mazut, shows significant material loss in the belly, partially exposing its hollow interior.

For these figurines, the examination of the internal structure is essential for making targeted decisions during digital restoration and for simulating their future behavior, but to also shed light on the reasons for the material degradation.

3.2. The Selection and Preparation of the Figurines

The selection of the aforementioned figurines was based on three specific parameters. The first parameter concerns their preservation state, as the severe pathology of the chosen figurines must still allow their safe transportation. The second parameter involves the examination of figurines made from different materials (wax, plasticine, mazut). The third and decisive parameter is the size of the figurines relative to the aperture of the available CT scanner. The selection of the objects was made in collaboration with the workshop conservator, who undertook the entire preparation and packaging process, supervised the transport, unpacking, placement in the CT scan, and ensured their safe return and placement back to their original positions.

As stated in relevant publications [17,27], the transport of the objects from the workshop to the diagnostic center and back required careful planning and preparation, including packing and unpacking the objects, selecting the route, considering time, day, and temperature, and checking the preservation state before and after transport, among other factors. The figurines were placed in cardboard boxes on specially designed braces, wrapped in acid-free paper, to ensure their safe transportation.

3.3. Equipment and Scan Parameters

The CT scan was conducted using a medical BrightSpeed 16 Slice CT Scanner, manufactured by GE HealthCare, and the scan was performed in Athens, Greece. The scanning parameters were set as follows: tube voltage: 120 kV, tube current: 35 mA, slice thickness: 0.625 mm, pitch: 0.938:1, rotation time: 1 s/cycle, matrix: 512 × 512; DICOM files were obtained (Appendix A).

The figurines were placed upright except for EPG_972, which was examined in both vertical and horizontal positions. The height of EPG_672 did not allow a complete scan, so a portion of its base was “cut off” in the imaging. The examination table’s straps were secured to the wooden base of the figurines, with thin strips of acid-free paper between the strap and the wooden base.

3.4. Software

The study and processing of the raw data were carried out in RadiAnt™ DICOM Viewer 2023.1 (trial version) in a Windows environment [77]. The software selection among the various available was based on its user-friendliness, its ability to measure Hounsfield Units (HU) in specified regions, and its automatic creation and export of three-dimensional models, without the need for additional plug-ins. During 3D reconstruction, the software provides windowing capabilities to focus on desired structures (window width—WW and window length—WL), the removal of unwanted elements, measurements, and exports in .stl format.

The data analysis was conducted in two stages. Initially, the internal structure of the models was examined, and the absorption of different construction materials was calculated. Subsequently, 3D models were extracted and further edited.

3.5. Material HU Density Values

The scout images provided an initial overview of the internal structure of the examined figurines and continued in the environment of multiplanar reconstruction (MPR). Initially, we recorded the relation and interconnection of the armature elements, along with the measurement of the wire’s diameters. Subsequently, we identified region-of-interest (ROI) areas, with different densities corresponding to different construction materials in

order to obtain Hounsfield Unit (HU) values. The absorption values of the materials were determined through multiple measurements at different levels per figurine and material, using the HU tool (oval selection area), and included the maximum and minimum absorption values, mean, standard deviation, and area size. The mean absorption values and standard deviation (SD) were calculated, as well as, in accordance with Spennemann and Singh [18], the weighted mean absorption, which takes into account the area of measurement. These multiple values were summarized by material per figurine (Table 1), and further summarized by material (Table 2). The mean and average mean values had similar results.

Table 1. Summary table of HU values by material for each figurine.

Figurine	Material	HU Range			Mean and SD—Weighted Mean		
EGP_962 (xnph)	Wax	−31	-	−108	−65	±8.6	−65
	Plasticine	1242	-	1188	1360	±29.4	1362
	Silicon	Measurement inability					
	Wooden base	−467	-	−771	−655	±54.0	−653
	Armature: Main wire	3071	-	2723	3052	±38.6	3060
	Wire	3071	-	1727	3068	±7.3	3071
	Nail	3071	-	3071	3071	±0.0	3068
Head fragment	Wax	−27	-	−127	−88	±17.5	−99
	Plasticine	1770	-	1404	1729	±80.7	1795
	Armature	3071	-	3071	3071	±0.0	3071
EGP_102 (old man)	Wax	6	-	−163	−68	±23.2	−67
	Plasticine	1342	-	1096	1249	±39.4	1249
	Wooden base	−338	-	−742	−590	±64.4	−589
	Armature: Wire	3071	-	2604	3062	±23.4	3052
	Nail	3071	-	3071	3071	±0.0	3071
	Plaster	554	-	103	412	±35.2	414
Hand fragment	Wax	−20	-	−137	−56	±15.1	−58
	Plasticine	1463	-	1043	1386	±33.8	1374
	Armature: wire	3071	-	3071	3071	±0.0	3071
EGP_XA (small Alex)	Mazut	−21	-	−175	−62	±13.7	−63
	Armature: Wire	3071	-	2771	3069	±4.1	3069
	Vertical stand	3071	-	3065	3071	±0.0	3071
	Nails	3071	-	3071	3071	±0.1	3071
	Wooden base A1	−285	-	−379	−340	±12.3	−339
	A2	−355	-	−492	−425	±22.3	−426
	B1	−319	-	−421	−366	±17.0	−368
	B2	−355	-	−495	−424	±19.7	−420
Fragments	Mazut	−8	-	−109	−62	±16.7	−64
	Armature	3071	-	2720	3068	±14.0	3068

Table 1. Cont.

Figurine	Material	HU Range		Mean and SD—Weighted Mean			
EGP_ 672 (large Alex)	Plasticine	961	-	-681	858	36.5	862
	Wooden base:						
	A1	-500	-	-746	-611	±27.2	-618
	A2	-451	-	-734	-598	±40.0	-607
	A3	-471	-	-605	-556	±17.2	-586
	A4	-362	-	-619	-519	±31.0	-512
	Armature:						
	Horizontal E1	3071	-	2384	3069	±7.3	3070
	Horizontal E2	3071	-	3071	3071	±0.0	3071
	Vertical stand	3071	-	2350	2918	±139.1	2918
	Binding wire	3071	-	1557	3024	±54.4	3010
	Wires (radial)	3071	-	2620	3070	±3.0	3070
	Wires ø 1.4–1.6	3071	-	2403	3061	±26.2	3058
	Restoration pins	3071	-	1915	2919	±104.6	2968
EGP_ 197 (cat)	Mazut	-22	--	-90	-56	±6.7	-55
	Wooden base	-426	-	-788	-637	±40.6	-581
	Wooden vertical element	-309	-	-520	-426	±39.1	-444
	Wooden horizontal element	-399	-	-522	-466	±15.5	-462
	Wooden spine reinforcement	510	-	-203	116	±29.3	117
	Armature:						
	Wire	3071	-	3071	3071	±0.0	3071
	Nails	3071	-	3071	3071	±0.0	3071
	Plaster	1018	-	260	663	±89.4	669
	Element on cat's head	1569	-	743	1284	±83.3	1238

Table 2. Summary table of HU values by material.

Material	Mean Value	Standard Deviation
Wax	-69	±13
Plasticine	1431	±46
Plasticine in EGP_672	858	±36
Mazut	-60	±12
Wooden elements	-509	±31
Metallic elements	3061	±10
Plaster	637	±62

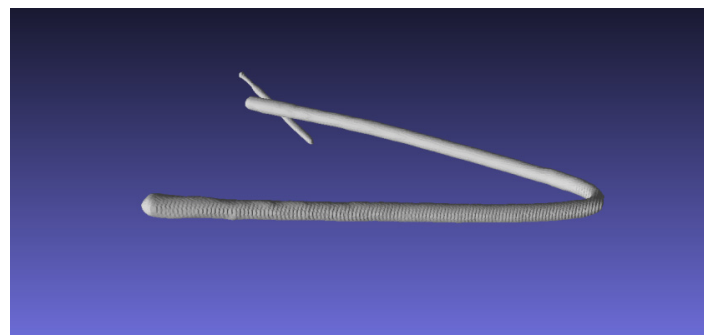
3.6. Three-Dimensional Reconstruction

In RadiAnt™, the 3D reconstruction is automated, based on the absorption values (HU) determined for each material. The values are defined either by the maximum and minimum HU values or by setting the mean HU value (WL refers to the midpoint HU value range) and width (WW refers to the range of HU represented). Since the construction materials have distinctly separate absorption ranges, as stated in Table 3, the result was

accurate, robust, and quick, with only minor adjustments. For each adsorption range we obtained 3D models of all the materials it included, in .stl format (Figure 2). To isolate and obtain 3D models of each construction material, Boolean operations were applied. Consequently, from the metal armature and the plasticine model, the metal armature model was subtracted to acquire the 3D model of plasticine, and so on.

Table 3. HU values in WL–WW used for the extraction of 3D models in .stl format.

Figurine	WL-WW	Materials Included in the 3D Model
EGP_962 (xnph)	–70–144	Metallic armature, plasticine, wax
	1178–100	Metallic armature, plasticine
	3071–50	Metallic armature
Fragment (head)	–108–132	Metallic armature, plasticine, wax
	1100–140	Metallic armature, plasticine
	3071–50	Metallic armature
EGP_102 (old man)	–294–181	All materials, not wood with noise
	–100–200	Metallic armature, plasticine, wax
	1200–400	Metallic armature, plasticine
	3071–50	Metallic armature
Fragment (arm)	–150–100	Metallic armature, plasticine, wax
	1200–300	Metallic armature, plasticine
	3071–50	Metallic armature
EGP_XA (small Alex)	–62–200	Metallic armature, mazut
	2936–272	Metallic armature
Fragments	–100–200	Metallic armature, mazut
	3061–12	Metallic armature
EGP_672 (large Alex)	0–200	Metallic armature, plasticine
	860–200	Metallic armature, part of plasticine
	3071–200	Metallic armature
EGP_197 (cat)	–500–12	Metallic armature, plaster, spine, mazut, wood
	–139–16	Metallic armature, plaster, spine element, mazut
	116–29	Metallic armature, plaster, spine element, and noise
	663–100	Metallic armature, plaster
	3071–100	Metallic armature



(a)

Figure 2. Cont.

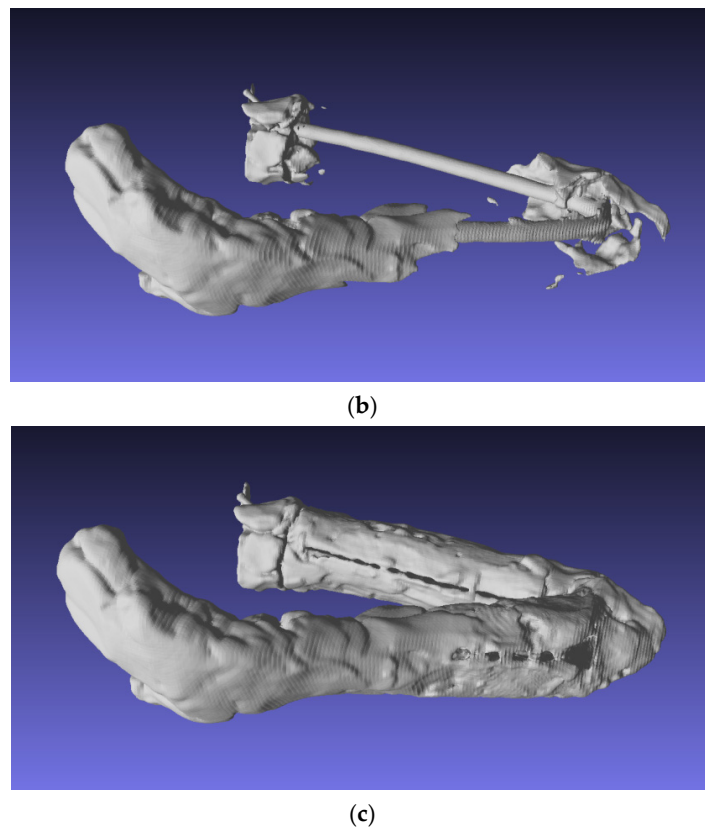


Figure 2. Initial reconstructed 3D models of armature (a), armature and plasticine (b), armature, plasticine, and wax (c) of EGP_102 detached arm.

The post-processing of the extracted 3D models was performed in MeshLab [78] and included the mesh cleaning and surface refinement of the model. Cleaning involved the removal of unnecessary elements, isolated pieces (diameter 5%), unreferenced vertices and T-vertices, and the repair of non-manifold edges. The modeling process created tunnels, which were identified and repaired by selecting and removing vertices, filling the area (cap hole) and removing residue isolated pieces.

The surfaces of all the 3D reconstruction models appear 'jagged' due to the voxel size of the slices (0.625 mm) as several other researchers have reported [64,66,67,73]. This size determines the accuracy of the final model [68]. MeshLabs's Laplacian Smooth (surface-preserving) filter reduced the jag, but in some cases the local micro-intervention using Blender® 4.1 digital sculpting tools was also necessary (Figure 3).

The metallic elements of the armature were painted so as to facilitate their study (Figure 3). Before proceeding to the next step, the 3D reconstruction models were aligned with the photogrammetry-generated 3D models using the ITC align feature in Meshlab (Figure 4).

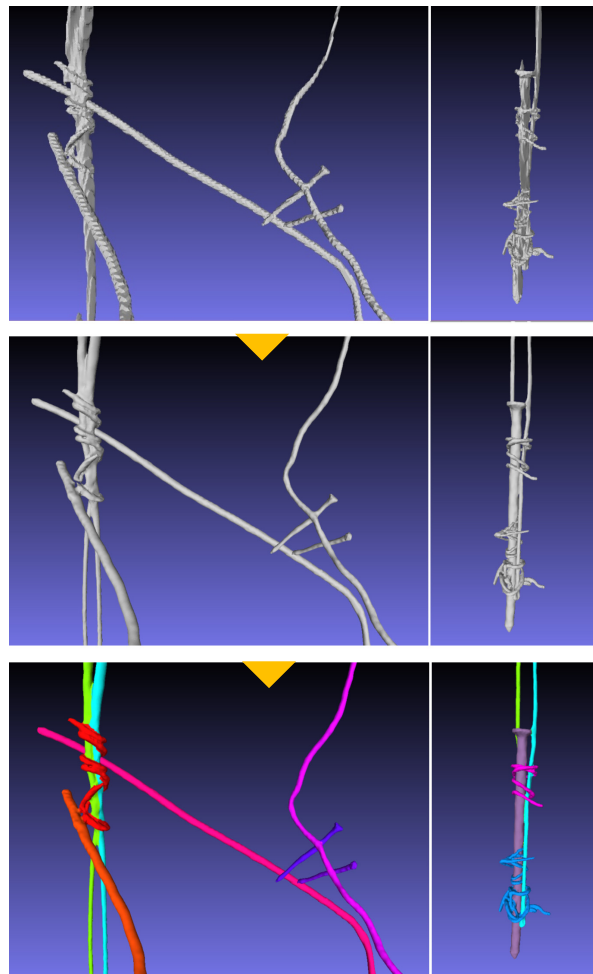


Figure 3. Post- processing of jagged areas and color application per wire, in 3D model of EGP_102.

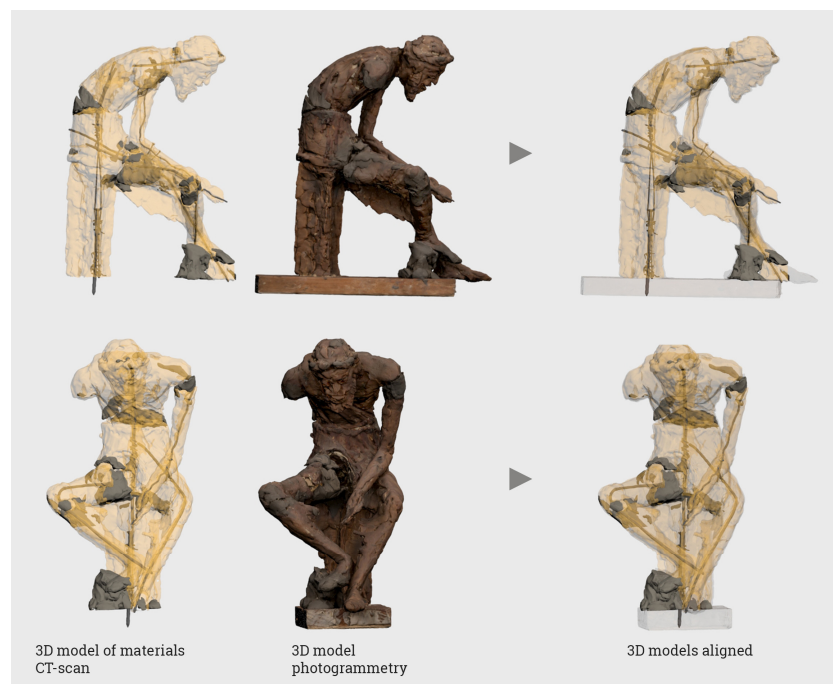


Figure 4. The integration of the 3D models of the structure materials to the photogrammetry-generated 3D model.

The metallic streak and other CT scan artifacts impeded the reconstruction of clean 3D models. In most cases, we were able to overcome this issue in the 3D reconstruction of the metallic elements with minor adjustments in the WW value. In two cases, the 3D reconstruction of the metallic structure appeared deformed or fragmentary, though it was clearly depicted in the scout file (see vertical wire EPG_102 and central support EPG_672, Figure 5(a1,a2)). In the first case, the missing part of the central wire was partially replaced by an equivalent that was designed and modeled according to the scout file in Blender (Figure 5(b1)). In the second case, the missing part was copied from the existing 3D photogrammetry model, as it is visible and therefore recorded (Figure 5(b2)). The most difficult case concerned EPG_XA, whose vertical support has not been clearly rendered (Figure 6a). The scout file provides a clear image of the element (Figure 6b) and the scans, assisting in the determination of its shape. This element has a complicated form that falls into the broader category of metal suspension/anchor plugs, perhaps a (self-)expanding girdle. We attempted semi-automated segmentation in 3D slicer, a time-consuming procedure as it required user intervention in each scan, with an outcome more or less similar and not acceptable. Therefore, we tried two different approaches utilizing the data from the scout image and sequential scans; in the first, the existing central support element was isolated and edited (sculpted) (Figure 6c) and in the second, the element was re-designed from scratch in Blender (Figure 6d).

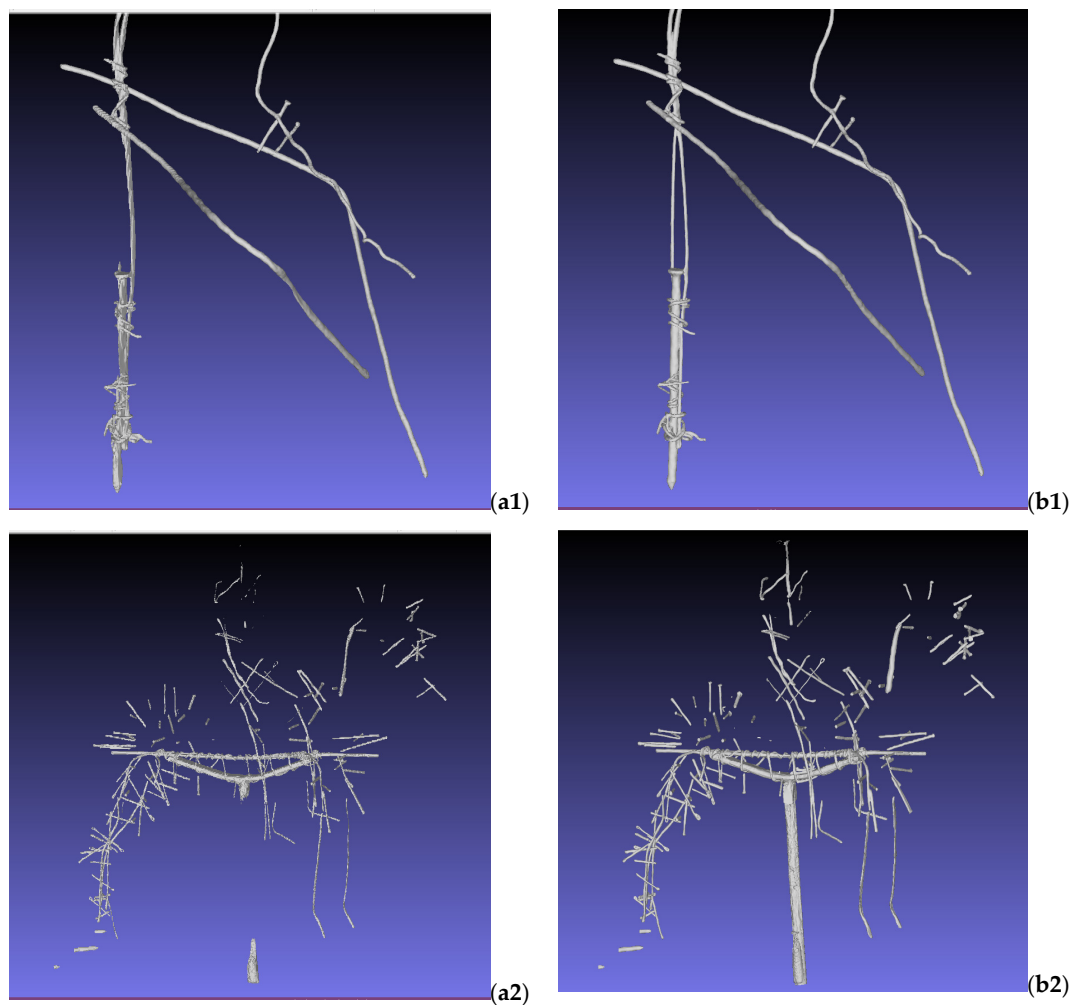


Figure 5. Initial (a1,a2) and final 3D models (b1,b2) of EPG_672 and EPG_102 armatures.

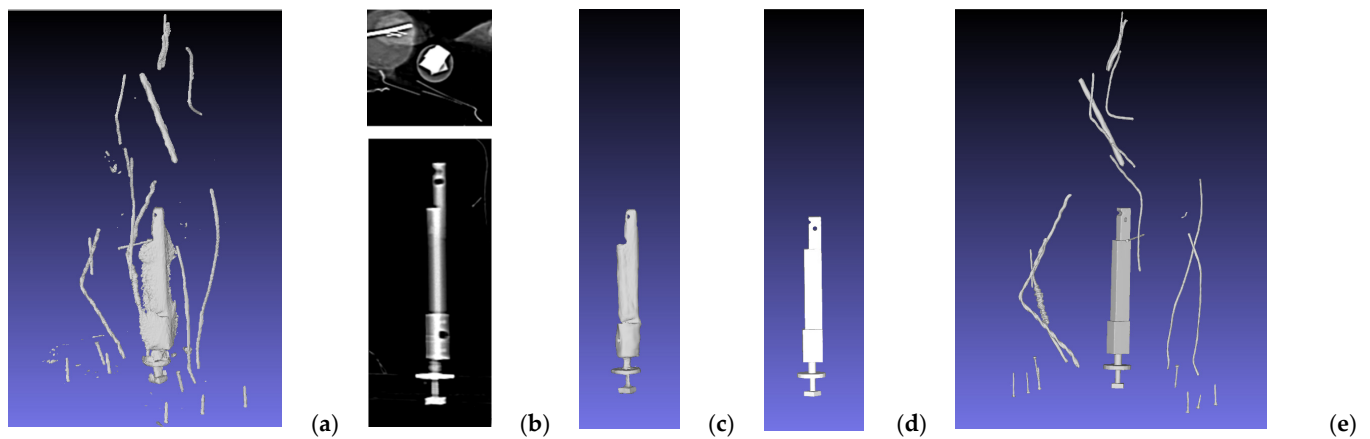


Figure 6. Initial and final 3D models of EGP_XA armature (a,e) and details of problematic vertical stand, scout file (b), edit of initial 3Dmodel (c), and re-designed model (d).

During the modeling of the organic materials, the CT's artifacts were visualized either as linear excesses (resulting from the included armature) or as indentations (Figure 2c), especially in the wax and mazut models. In most cases, the isolation of each material reduced the excess to their small contact region, easily corrected by deleting the excess area and filling the region. The indentations were not treated, as they cover long, elongated areas and their correction demands extensive intervention. Instead, a 3D model of the wax or mazut could be created by the subtraction of the CT's 3D models of all other materials from the photogrammetry's 3D model.

3.7. WebGL Presentation and Manipulation

The availability of the final digital 3D models also enables their porting to the WebGL platform. WebGL represents an API for 3D graphics rendering [79], typically hosted by HTML/Javascript, natively supported by all modern popular web browsers. The latter fact implies the elimination of the need for any required plugins and additional tools for the presentation and manipulation of 3D web content, thus minimizing the relevant computational footprint and overhead. These characteristics make WebGL-based visual web applications instantly accessible to a wide range of handheld, portable, and desktop devices and relevant system platforms, increasing the potential for collaboration as well as the dissemination and appreciation of produced results, while maintaining the minimal requirements for the 3D graphics content functionality offered.

Porting the 3D models to the Javascript/WebGL platform also allows significant flexibility in their further digital exploitation and exploration, opening additional paths for harnessing their computational potential. Such functionality can involve the exploration of alternative deformation paths, from the initial known state to the current recorded one, through the definition of one or more intermediate states. This exploration may rely on the properties of the malleable materials for the plastic deformations of the objects, in regard to the computational part, while presenting these deformations through morphing between defined states, in regard to the visual part, in a manner similar to the approach presented for human body deformation [80], offering user control of the speed, granularity, and other custom parameters of morphing. This section may be divided by subheadings. It should provide a concise and precise description of the experimental results, their interpretation, as well as the experimental conclusions that can be drawn.

4. Results

The artist used wires of $\varnothing 1.4$ – 1.6 mm and $\varnothing 0.4$ – 0.6 mm to give the general shape to the figurines. The central element consists of one or two single wires \varnothing while the limbs consist of thinner wires, often interwinding. The metal elements remain unconnected to each other, and they barely penetrate the wooden base, as shown in Figure 1.

In more detail, in the EGP_972 figurine, two unconnected metal wires form the body, while the legs are reinforced with two nails, which penetrate the wooden base. The arms are formed from thinner, single wires, reinforced by winding wires in the upperarm area. On the head, a thinner wire is wrapped around the central one, at the area of the neck.

The central element of EGP_102 figurine's armature is formed by two metal wires tied together at waist height and with the interposed nail at seat height. The legs, arms, and head are formed using single wires. The right arm is attached to the thigh with two thin nails.

The armature of the EGP_672 figurine includes a metal stand joined to a bent metal element that runs across the horse's belly. In the second, a metal rod and two wires are tied, which extend and form the upper part of the horse's legs. The lower part of the horse's legs, as well as the limbs and torso of the rider, and the horse's neck, are formed by single wires, reinforced in some places by secondary wires or self-braided. Short metal elements were placed radially towards the mass of the material, one side of which is visible on the final surface of the figurine.

In the EGP_XA figurine, the metal stand is not connected to any other reinforcing element. The limbs of the horse and the rider are formed by a single wire, which in the case of the rear leg is short and therefore tied with a second complementary element. The horse's neck and head do not have any reinforcement.

In the case of the EGP_197 figurine, the armature consists of a wooden stand connected to the base and the elongated horizontal wooden element that runs down the spine by the use of plaster. A wire attaches the tail to the main body.

As stated beforehand, the accuracy of the 3D reconstructed models is 0.625. The mean ground sampling distance is approx. 0.1 mm/pixel [81] and the accuracy approx. 0.2 mm [2].

5. Discussion

The Hounsfield values (HU) for each material, even for malleable organic materials, are distinct and fall within the same absorption area, with a small standard deviation. Mazut and wax have more or less similar values, while plasticine differs. The HU value of EGP_672's plasticine differs significantly from the plasticine of the other figurines, something that requires further investigation.

The recorded absorption values of materials in the literature are stated in Table 4 and consist mostly of HU values for the characterization of foreign elements in the human body [82,83]. In most of these measurements, the metallic elements have a peak at 3071, with steel, copper, and silver differing in their in-between measurements. Absorption appears to depend on the atomic number, as stated by Paulis et al. [84], and therefore the values of alloys differ significantly from each other [85]. Our metallic elements, with an HU value of 3061 ± 10 , could be alloys, with an atomic number around 74. Artists use all kinds of materials in the armature: iron, steel stainless steel, aluminum, copper, etc. Degas, for example, used lead pipes in the armature of the little dancer [4]. The visible metallic elements in the examined figurines refer to iron or iron alloys. Iron's atomic number is 26; if the alloy contains a metal with a higher value, such as tungsten with an atomic number of 74, then the resulting material will exhibit in the HU a combination of properties from both elements.

Non-metallic materials such as wax and plasticine are not listed in the literature. Asphalt, at 225 ± 109 [82], as a petroleum derivative, could be compared to the figurine's mazut, and indeed their absorption values are relatively close. Wood, at 464 [82], approximates our measurements at 509, though it would be interesting to identify the broadest or most specific category of wood according to absorption, as there are measurable variations in the HU measurements.

Table 4. Recorded material absorption values (HU) in the literature.

Material	Range of CT Numbers (HU)	Average of CT Numbers (HU)
Stainless steel	1071–3071 ^A	2222 ± 737 ^A
Steel	1972–2249 ^B	2034 ± 63 ^B
Titanium	2840–3071 ^A	2921 ± 218 ^A
Gold	2748–3071 ^A 3071 ^B	2908 ± 325 ^A 3071 ± 0 ^B
Copper	2812–3071 ^A	2909 ± 228 ^A 1403 ± 537 ^B
Brass	2696–3071 ^B	3067 ± 145.3 ^B
Lead	1901–3071 ^A	2758 ± 539 ^A 3067 ± 83 ^B
Silver	3065–3071 ^A	3069 ^A 1695 ± 248 ^B
Aluminum	223–248 ^B	233 ± 24 ^B
HU adsortion in regard to the atomic number of metals ^C :		
Z ≤ 13 (Aluminum (3–5% Cu)):		HU < 300
Z = 25–30 (Iron; Stainless steel; Coper; Brass (60–80% Cu; 20–40% Zn)		HU = 1300–2000
Z ≥ 74 (Tungsten; Lead)		HU > 3000
Silicon	195–755 ^A	278 ± 120 ^A
Glass	105–2093 ^A	947 ± 523 ^A
Glass (bottle)	199–241 ^B	209 ± 41 ^B
Glass (window)	330–810 ^B	49 ± 56 ^B
Medpor	19–53 ^A	32 ± 5 ^A
Stone	735–1832 ^A	1320 ± 280 ^A
Limestone	252–294 ^B	276 ± 41 ^B
Marble	181–278 ^B	229 ± 82 ^B
Shale	182–267 ^B	221 ± 33 ^B
Granite	173–283 ^B	213 ± 110 ^B
Quartzite	142–193 ^B	175 ± 40 ^B
Sandstone	140–191 ^B	163 ± 42 ^B
Asphalt	152–299 ^B	225 ± 109 ^B
Cement	75–196 ^B	142 ± 82 ^B
Tile	144–174 ^B	155 ± 15 ^B
Pottery	124–158 ^B	142 ± 18 ^B
Polystyrene	–62–35 ^A	–47 ^A
Wood	–437–491 ^A	–464 ^A

Where A: Choi et al., 2010 [83], B: Bolliger et al., 2009 [82], C: Paulis et al., 2019 [84].

During HU measurements, we noticed small “discontinuities” in the material mass that could be attributed to small air bubbles, impurities, or incomplete mixing during the creation of the mixture; HU measurements in small elements, even when pinpointed, were easily contaminated by the HU of neighbor materials, expressed as a high standard deviation, e.g., in EGP_672’s restoration pins or the small plasticine or silicon in EGP_197’s head. To avoid this, especially in the wires, the measurements were made on their diameter sections.

The use of disconnected metallic elements coincides with the very nature of the figurines and the logic of experimentation, as the artist wanted to explore different poses of the theme. However, the combination of pliable, sensitive materials and a “weak” internal framework enhances the plastic deformations and instability, a hypothesis that will be further investigated. The artists were aware of this and produced plaster copies of the artworks they wished to preserve, and less frequently bronze ones.

The three-dimensional models of the armature will be utilized during the restoration of the plastic deformations of the figurines and the repositioning of the members. In

closing, however, we would like to give a brief insight into the utilization of the isolated materials models in the reverse study of the EGP_102 figurine. The digital removal of plasticine's additions from the shoulders and right thigh resulted in matching wax surfaces, and therefore verified that the limbs of the figure have been lengthened. On the back of the figure, part of the plasticine has detached from the wax, as a consequence of the evolution of the inclination of the torso, revealing a deep flat wax surface as if the figurine has been cut to create the torso's leaning, and the gap was filled with plasticine. This hypothesis was verified by examination of the "pure" wax 3D model, as the upper and lower area of the cut match completely, and the posture of the old man matches that of a bronze figurine, similar, but quite different.

The workflow developed is both simple and accessible, leveraging open-source software to support conservators in their work. One of the limitations in using CT scans is their limited accessibility and the potential risk of worsening the preservation state of fragile objects. So, successful implementation requires time-consuming preparation. The resolution of a medical-grade CT scanner (0.625 mm) is relatively low compared to photogrammetry (0.2 mm); however, the spatial information revealed by CT scans is invaluable for the documentation, preservation, and restoration of objects. In some cases, incomplete data capture for certain metal structures due to artifacts could potentially be mitigated with the option to rescan using different parameters. For the figurines, as part of the preparation for the next simulation stage, these areas were corrected in two cases and partially replaced by photogrammetry's model in one case. Furthermore, distinguishing materials with similar absorption properties remains challenging, where human expertise plays a crucial role in making the correct selection. Many of these limitations are common across various 3D recording methods, requiring repeated scans and appropriate settings. Nevertheless, the benefits of scanning, particularly the acquisition of volumetric data about the internal structure, far outweigh these challenges.

Author Contributions: Conceptualization, C.S., D.M. and G.B.; methodology, C.S., D.M. and G.B.; software, C.S., D.M. and G.B.; validation, C.S., D.M. and G.B.; formal analysis, C.S.; resources, C.S.; data curation, C.S.; writing—original draft preparation, C.S., D.M. and G.B.; writing—review and editing, C.S., D.M. and G.B.; visualization, C.S.; supervision, D.M. All authors have read and agreed to the published version of the manuscript.

Funding: The publication of this article was financially supported from the Special Account for Research Grants of the University of West Attica.

Data Availability Statement: All data of digital 3D models is unavailable due to privacy.

Acknowledgments: The authors would like to acknowledge the Yannis Pappas Studio—Benaki Museum, and especially Alekos Pappas and conservator Christine Hollinetz, for graciously providing the authentic artworks, along with their hospitality and facilitation in the conduct of the study.

Conflicts of Interest: The authors declare no conflicts of interest.

Appendix A

Table A1. Acquired files from CT Scan.

Figurine	Series	Image Data		
EPG_972 (<i>xenofanis vertical</i> –36073)	06/05/2023, 1:22:47 $\mu.\mu.$ CT, SCOUT MODE	888 × 486 × 2 voxels	0.55 × 0.60 × 265.64 mm	Original
	06/05/2023, 1:45:40 $\mu.\mu.$ CT, HELICAL MODE	512 × 512 × 561 voxels	0.90 × 0.90 × 0.62 mm	Original
EPG_972 (<i>xenofanis head</i> –36073)	06/05/2023, 1:28:45 $\mu.\mu.$ CT, SCOUT MODE	888 × 184 × 2 voxels	0.55 × 0.60 × 100.55 mm	Original
	06/05/2023, 2:00:10 $\mu.\mu.$ CT, HELICAL MODE	512 × 512 × 169 voxels	0.27 × 0.27 × 0.62 mm	Original

Table A1. Cont.

Figurine	Series	Image Data		
EPG_XA (alexandros small–36075)	06/05/2023, 2:12:46 $\mu.\mu.$ CT, SCOUT MODE	888 × 413 × 2 voxels	0.55 × 0.60 × 225.64 mm	Original
	06/05/2023, 2:14:37 $\mu.\mu.$ CT, HELICAL MODE	512 × 512 × 384 voxels	0.81 × 0.81 × 0.62 mm	Original
EPG_XA (alexandros parts–36076)	06/05/2023, 2:28:53 $\mu.\mu.$ CT, SCOUT MODE	888 × 404 × 2 voxels	0.55 × 0.60 × 220.55 mm	Original
	06/05/2023, 2:28:53 $\mu.\mu.$ CT, HELICAL MODE	512 × 512 × 306 voxels	0.45 × 0.45 × 0.62 mm	Original
EPG_102 (old man–36077)	06/05/2023, 2:38:51 $\mu.\mu.$ CT, SCOUT MODE	888 × 613 × 2 voxels	0.55 × 0.60 × 334.55 mm	Original
	06/05/2023, 2:40:57 $\mu.\mu.$ CT, HELICAL MODE	512 × 512 × 379 voxels	0.70 × 0.70 × 0.62 mm	Original
EPG_102 (old man hand–36078)	06/05/2023, 2:47:11 $\mu.\mu.$ CT, SCOUT MODE	888 × 321 × 2 voxels	0.55 × 0.60 × 175.64 mm	Original
	06/05/2023, 2:48:42 $\mu.\mu.$ CT, HELICAL MODE	512 × 512 × 215 voxels	0.24 × 0.24 × 0.62 mm	Original
EPG_672 (alexandros large –33079)	06/05/2023, 2:53:51 $\mu.\mu.$ CT, SCOUT MODE	888 × 770 × 2 voxels	0.55 × 0.60 × 420.55 mm	Original
	06/05/2023, 2:56:56 $\mu.\mu.$ CT, HELICAL MODE	512 × 512 × 605 voxels	0.89 × 0.89 × 0.62 mm	Original
EPG_197 (cat-36080)	06/05/2023, 3:03:11 $\mu.\mu.$ CT, SCOUT MODE	888 × 1550 × 2 voxels	0.55 × 0.60 × 845.64 mm	Original
	06/05/2023, 3:05:05 $\mu.\mu.$ CT, HELICAL MODE	512 × 512 × 1379 voxels	0.70 × 0.70 × 0.62 mm	Original
	06/05/2023, 3:06:52 $\mu.\mu.$ CT, HELICAL MODE	512 × 512 × 41 voxels	0.70 × 0.70 × 5.00 mm	Original

References

- Benaki Museum. The Yannis Pappas Studio. Available online: https://www.benaki.org/index.php?option=com_buildings&view=building&id=5&Itemid=138&lang=el (accessed on 21 June 2024).
- Sakellariou, C.; Makris, D.; Karampinis, L. A Digital Study of the Morphological and Stability Issues of a Delicate Wax-based Artwork. *Stud. Conserv.* **2022**, *68*, 474–489. [\[CrossRef\]](#)
- Rich, J.C. *The Materials and Methods of Sculpture*; Dover Publications: New York, NY, USA, 1988.
- National Gallery of Art (NGA). Little Dancer Internal Construction. Article from the Catalog Edgar Degas Sculpture. 2010. Available online: <https://www.nga.gov/features/modeling-movement/degas-internal-construction.html> (accessed on 21 June 2024).
- Hughes, S. CT Scanning in Archaeology. In *Computed Tomography—Special Applications*; Saba, L., Ed.; IntechOpen: Rijeka, Croatia, 2011; pp. 57–70. [\[CrossRef\]](#)
- Auferherder, A. *The Scientific Study of Mummies*; Cambridge University Press: Cambridge, UK, 2003; Available online: <https://assets.cambridge.org/97805218/18261/sample/9780521818261ws.pdf> (accessed on 21 June 2024).
- Cox, S. A Critical Look at Mummy CT Scanning. *Anat. Rec.* **2015**, *298*, 1099–1110. [\[CrossRef\]](#) [\[PubMed\]](#)
- Cosmacini, P.; Piacentini, P. Notes on the history of the radiological study of Egyptian mummies: From X-rays to new imaging techniques. *Radiol. Med.* **2008**, *113*, 615–626. [\[CrossRef\]](#) [\[PubMed\]](#)
- Maravelia, A.; Bontozoglou, N.; Kalogerakou, K.; Couvaris, C.M.; Geroulanos, S. Application of smart infogramatics in Egyptology: The Athens mummy project as an example of effective interdisciplinary. *Orient. Stud.* **2019**, *84*, 127–169. [\[CrossRef\]](#)
- Lynnerup, N. Medical Imaging of Mummies and Bog Bodies—A Mini-Review. *Gerontology* **2010**, *56*, 441–448. [\[CrossRef\]](#)
- Bibb, R.; McKnight, L. Identification of bird taxa species in ancient Egyptian mummies: Part 2, a qualitative evaluation of the utility of CT scanning and 3D printing. *J. Archaeol. Sci. Rep.* **2022**, *46*, 103668. [\[CrossRef\]](#)
- Sutherland, M.L. Use of Computed Tomography scanning in a ‘virtual’ bioarchaeology of care analysis of a Central Coast Peruvian mummy bundle. *Int. J. Paleopathol.* **2019**, *25*, 129–138. [\[CrossRef\]](#)
- Ventura, L.; Fornaciari, G.; Calabrese, A.; Arrizza, L.; Fornaciari, A. Paleopathology of a 19th century mummy of a nobleman from Popoli, central Italy. *Med. Hist.* **2020**, *4*, 29–34.
- Coppa, A.; Bondioli, L.; Cucina, A.; Frayer, D.W.; Jarrige, C.; Jarrige, J.-F.; Quivron, G.; Rossi, M.; Vidale, M.; Macchiarelli, R. Early Neolithic tradition of dentistry Flint tips were surprisingly effective for drilling tooth enamel in a prehistoric population. *Nature* **2006**, *440*, 755–756. [\[CrossRef\]](#)

15. Piombino-Mascalì, D.; Jankauskas, R.; Zink, A.R.; Sergio Todesco, M.; Aufderheide, A.C.; Panzer, S. Paleoradiology of the Savoca Mummies, Sicily, Italy (18th–19th Centuries AD). *Anat. Rec.* **2015**, *298*, 988–1000. [[CrossRef](#)]
16. Ventura, L.; Bruno, F.; Barile, A. Bilateral fabella in the mummy of the Blessed Jean Bassand (c.1360-1445). A unique description in ancient human remains. *Int. J. Osteoarchaeol.* **2021**, *31*, 1276–1279. [[CrossRef](#)]
17. Karapanagiotou, A.V.; Lazaris, P.; Grigoraki, A.; Nikolentzos, K. The collection of Egyptian antiquities in the National Archaeological Museum and the Athens mummy project: A preliminary report. *J. Hell. Inst. Egyptol. (JHIE)* **2021**, *4*, 29–40. [[CrossRef](#)]
18. Spennemann, D.H.R.; Singh, C.L. Computed Tomography Analysis of the Manufacture of Cast Head-Bust Figurines by Patricia ‘Pat’ Elvins (1922–2011). *Heritage* **2023**, *6*, 2268–2291. [[CrossRef](#)]
19. Sowada, K.; Davey, J. Computerised Tomography (CT) scans of a mummified male head from the Ptolemaic period. In *Guardian of Ancient Egypt Studies in Honor of Zahi Hawass Volume III*; Kamrin, J., Bárta, M., Ikram, S., Lehner, M., Megahed, M., Eds.; Charles University in Prague: Prague, Czech Republic, 2020; pp. 1511–1526.
20. Yatsishina, E.B.; Vasilyev, S.V.; Vasilieva, O.A.; Galeev, R.M.; Dyuzheva, O.P.; Kovalchuk, M.V. CT-Scanning Analysis of the Inner Structure of Ancient Egyptian Mummy. *Crystallogr. Rep.* **2020**, *65*, 1064–1072. [[CrossRef](#)]
21. Longo, S.; Mormina, E.; Granata, F.; Mallamace, D.; Longo, M.; Capuani, S. Investigation of an Egyptian Mummy board by Using Clinical Multi-slice Computed Tomography. *Stud. Conserv.* **2018**, *63*, 383–390. [[CrossRef](#)]
22. Maher, M.A. X-ray computed tomography of a late period falcon bronze coffin. *Radiat. Phys. Chem.* **2019**, *166*, 108475. [[CrossRef](#)]
23. Minozzi, S.; Giuffra, V.; Bagnoli, J.; Paribeni, E.; Giustini, D.; Caramella, D.; Fornaciari, G. An investigation of Etruscan cremations by Computed Tomography (CT). *Antiquity* **2010**, *84*, 195–201. [[CrossRef](#)]
24. Saleem, S.N.; Seddik, S.A.E.; El-Halwagy, M. Scanning and three-dimensional-printing using computed tomography of the “Golden Boy” mummy. *Front. Med.* **2023**, *9*, 028377. [[CrossRef](#)]
25. Cesarani, F.; Martina, M.C.; Grilletto, R.; Boano, R.; Roveri, A.M.; Capussotto, V.; Giuliano, A.; Celia, M.; Gandini, G. Facial reconstruction of a wrapped Egyptian mummy using MDCT. *AJR Am. J. Roentgenol.* **2004**, *183*, 755–758. [[CrossRef](#)]
26. Morigi, M.P.; Casali, F.; Bettuzzi, M.; Brancaccio, R.; D’Errico, V. Application of X-ray Computed Tomography to cultural heritage diagnostics. *Appl. Phys. A* **2010**, *100*, 653–661. [[CrossRef](#)]
27. Bossema, F.; Coban, S.; Kostenko, A.; van Duin, P.; Dorscheid, J.; Garachon, I.; Hermens, E.; van Liere, R.; Batenburg, K. Integrating expert feedback on the spot in a time-efficient explorative CT scanning workflow for cultural heritage objects. *J. Cult. Herit.* **2021**, *49*, 38–47. [[CrossRef](#)]
28. Re, A.; Corsi, J.; Demmelbauer, M.; Martini, M.; Mila, G.; Ricci, C. X-ray tomography of a soil block: A useful tool for the restoration of archaeological finds. *Herit. Sci.* **2015**, *3*, 4. [[CrossRef](#)]
29. Albertin, F.; Bettuzzi, M.; Brancaccio, R.; Morigi, M.P.; Casali, F. X-Ray Computed Tomography In Situ: An Opportunity for Museums and Restoration Laboratories. *Heritage* **2019**, *2*, 2028–2038. [[CrossRef](#)]
30. Andonova, M. Ancient basketry on the inside: X-ray computed microtomography for the non-destructive assessment of small archaeological monocotyledonous fragments: Examples from Southeast Europe. *Herit. Sci.* **2021**, *9*, 158. [[CrossRef](#)]
31. Applbaum, N.; Applbaum, Y. The Use of Medical Computed Tomography (CT) Imaging in the Study of Ceramic and Clay Archaeological Artifacts from the Ancient Near East. In *X-rays for Archaeology*; Uda, M., Demortier, G., Nakai, I., Eds.; Springer: Dordrecht, The Netherlands, 2005; pp. 231–245. [[CrossRef](#)]
32. Sallam, A.M.; Hemeda, S.; Toprak, M.S.; Muhammed, M.; Hassan, M.; Uheida, A. CT Scanning and MATLAB Calculations for Preservation of Coptic Mural Paintings in Historic Egyptian Monasteries. *Sci. Rep.* **2019**, *9*, 3903. [[CrossRef](#)]
33. Morigi, M.P.; Casali, F.; Bettuzzi, M.; Bianconi, D.; Brancaccio, R.; Cornacchia, S.; Pasini, A.; Rossi, A.; Aldrovandi, A.; Cauzzi, D. CT investigation of two paintings on wood tables by Gentile da Fabriano. *Nucl. Instrum. Methods Phys. Res. Sect. A Accel. Spectrometers Detect. Assoc. Equip.* **2007**, *580*, 735–738. [[CrossRef](#)]
34. Casali, F.; Bettuzzi, M.; Bianconi, D.; Brancaccio, R.; Cornacchia, S.; Cucchi, C.; Di Nicola, E.; Fabbri, A.; Lanconelli, N.; Morigi, M.P.; et al. X-ray computed tomography of an ancient large globe. In *Optical Methods for Arts and Archaeology*; SPIE: Bellingham, WA, USA, 2005; Volume 5857. [[CrossRef](#)]
35. Badde, A.; Illerhaus, B. Three Dimensional Computerized Microtomography in the Analysis of Sculpture. *Scanning* **2008**, *30*, 16–26. [[CrossRef](#)]
36. Ghysels, M. CT Scans in Art Work Appraisal. 2005. Available online: <https://www.asianart.com/articles/ghysels/index.html> (accessed on 21 June 2024).
37. Karl, S.; Jungblut, D.; Mara, H.; Wittum, G.; Krömker, S. Insights into manufacturing techniques of archaeological pottery: Industrial X-ray computed tomography as a tool in the examination of cultural material. In *Craft and Science: International Perspectives on Archaeological Ceramics*, UCL Qatar Series in Archaeology and Cultural Heritage; Martínón-Torres, M., Ed.; Bloomsbury Qatar Foundation: Doha, Qatar, 2014; pp. 253–262. [[CrossRef](#)]
38. Kozatsas, J.; Kotsakis, K.; Sagris, D.; David, K. Inside out: Assessing pottery forming techniques with micro-CT scanning. An example from Middle Neolithic Thessaly. *J. Archaeol. Sci.* **2018**, *100*, 102–119. [[CrossRef](#)]
39. Lipkin, S.; Karjalainen, V.P.; Puolakka, H.L.; Finnilä, M.A. Advantages and limitations of micro-computed tomography and computed tomography imaging of archaeological textiles and coffins. *Herit. Sci.* **2023**, *11*, 231. [[CrossRef](#)]
40. Miles, J.; Mavrogordato, M.; Sinclair, I.; Hinton, D.; Boardman, R.; Earl, G. The use of computed tomography for the study of archaeological coins. *J. Archaeol. Sci. Rep.* **2016**, *6*, 35–41. [[CrossRef](#)]

41. Nemoto, A. June 2. CT Scan Reveals Tiny Statue inside Ancient Buddhist Workin Kyoto. The Asian Shimbun. 2020. Available online: <https://www.asahi.com/ajw/articles/photo/30729105> (accessed on 21 June 2024).
42. Vigorelli, L.; Re, A.; Guidorzi, L.; Brancaccio, R.; Bortolin, C.; Grassi, N.; Mila, G.; Pastrone, N.; Sacchi, R.; Grassini, S.; et al. The study of ancient archaeological finds through X-ray tomography: The case of the “Tintinnabulum” from the Museum of Anthropology and Ethnography of Torino. *J. Phys. Conf. Ser.* **2022**, *2204*, 012034. [[CrossRef](#)]
43. Klein, C. CT Scan Reveals Mummified Monk Inside Ancient Buddha Statue. History, 23 August 2023. Available online: <https://www.history.com/news/ct-scan-reveals-mummified-monk-inside-ancient-buddha-statue> (accessed on 21 June 2024).
44. Baumann, R.; Porter, C.D.; Seales, W.B. The use of Micro-CT in the study of archeological artifacts. In Proceedings of the 9th International Conference on NDT of Art, Jerusalem, Israel, 25–30 May 2008.
45. Bello, S.M.; De Groote, I.; Delbarre, G. Application of 3-dimensional microscopy and micro-CT scanning to the analysis of Magdalenian portable art on bone and antler. *J. Archaeol. Sci.* **2013**, *40*, 2464–2476. [[CrossRef](#)]
46. Sirr, S.A.; Waddle Luthier, J.R. Use of CT in detection of internal damage and repair and determination of authenticity in high quality bowed stringed instruments. *Radiogr. Sci. Exhib.* **1999**, *19*, 639–646. [[CrossRef](#)] [[PubMed](#)]
47. Bettuzzi, M.; Casali, F.; Morigi, M.P.; Brancaccio, R.; Carson, D.; Chiari, G.; Maish, J. Computed tomography of a medium size Roman bronze of Cupid. *Appl. Phys. A* **2015**, *118*, 1161–1169. [[CrossRef](#)]
48. Sabino, R.C.; Vannier, M.W. The Slice is Right: Medical Imaging for Authentication of West African Ceramics. In Proceedings of the Recent Advances in Glass and Ceramics Conservation 2019, Interim Meeting of the ICOM-CC Working Group, London, UK, 5–7 September 2019.
49. Björngrim, N.; Myronycheva, O.; Fjellström, P.A. The use of large-scale X-ray computed tomography for the evaluation of damaged structural elements from an old timber bridge. *Wood Mater. Sci. Eng.* **2022**, *17*, 1028–1029. [[CrossRef](#)]
50. Seguin, F.H. High resolution computed tomography and digital radiography of archaeological and art—Historical objects. *Mater. Res. Soc. Symp. Proc.* **1991**, *185*, 65–72. [[CrossRef](#)]
51. Ngan-Tillard, D.J.M.; Huisman, D.J.; Corbella, F.; Van Nass, A. Over the rainbow? Micro-CT scanning to non-destructively study Roman and early medieval glass bead manufacture. *J. Archaeol. Sci.* **2018**, *98*, 7–21. [[CrossRef](#)]
52. Bill, J.; Daly, A.; Johnsen, O.; Dalen, K.S. DendroCT—Dendrochronology without damage. *Dendrochronologia* **2012**, *30*, 223–230. [[CrossRef](#)]
53. Okochi, T. A non destructive dendrochronological study on wooden art sculptures using micro-focus X-ray Computed Tomography (CT) Reviewing two methods for scanning objects of different sizes. *Dendrochronologia* **2016**, *38*, 1–10. [[CrossRef](#)]
54. Daly, A.; Streeton, N.L.W. Non-invasive dendrochronology of late-medieval objects in Oslo: Refinement of a technique and discoveries. *Appl. Phys. A* **2017**, *123*, 431. [[CrossRef](#)]
55. Domínguez-Delmás, M.; Bossema, F.G.; van der Mark, B.; Kostenko, A.; Coban, S.B.; van Daalen, S.; van Duin, P.; Batenburg, K.J. Dating and provenancing the Woman with lantern sculpture—A contribution towards attribution of Netherlandish art. *J. Cult. Herit.* **2021**, *50*, 179–187. [[CrossRef](#)]
56. Wilson, P.F.; Smith, M.P.; Hay, J.; Warnett, J.M.; Attridge, A.; Williams, M.A. X-ray computed tomography (XCT) and chemical analysis (EDX and XRF) used in conjunction for cultural conservation: The case of the earliest scientifically described dinosaur *Megalosaurus bucklandii*. *Herit. Sci.* **2018**, *6*, 56. [[CrossRef](#)] [[PubMed](#)]
57. Bugani, S.; Camaiti, M.; Morselli, L.; Vande Castele, E.; Cloetens, P.; Janssens, K. X-ray computed tomography as a non-destructive tool for stone conservation. In Proceedings of the 9th International Conference on NDT of Art, Jerusalem, Israel, 25–30 May 2008.
58. Rankin, K.E.; Hazell, Z.J.; Middleton, A.M.; Mavrogordato, M.N. Micro-focus X-ray CT scanning of two rare wooden objects from the wreck of the London, and its application in heritage science and conservation. *J. Archaeol. Sci. Rep.* **2021**, *39*, 103158. [[CrossRef](#)]
59. Jansen, R.; Poulus, M.; Kottman, J.; de Groot, T.; Huisman, D.; Stoker, J. CT: A New nondestructive method for visualizing and characterizing ancient roman glass fragments in situ in blocks of soil. *Radiographics* **2006**, *26*, 1837–1844. [[CrossRef](#)]
60. Johnston, D. CT Scan for Free. Nautical Archaeological Society. Available online: <https://www.nauticalarchaeologysociety.org/ct-scan-for-free> (accessed on 21 June 2024).
61. Bettuzzi, M.; Brancaccio, R.; Casali, F.; Cornacchia, S.; Giordano, M.; Morigi, M.P.; Pasini, A.; Romani, D. Innovative systems for digital radiography and computed tomography: Applications to cultural heritage diagnostics. In *Physics Methods in Archaeometry*; Martini, M., Milazzo, M., Piacentini, M., Eds.; IOSPress: Amsterdam, The Netherlands, 2004; pp. 461–470.
62. Vasilyev, S.V.; Vasilyeva, O.A.; Galeev, R.M.; Dyuzheva, O.P.; Novikov, M.; Chichaev, I.A.; Yatsishina, E.B. 3D reconstruction of the ancient Egyptian mummy skeleton from the Pushkin state museum of fine arts(I,11240). *Int. Arch. Photogramm. Remote Sens. Spat. Inf. Sci.* **2019**, *XLII-2/W12*, 225–229. [[CrossRef](#)]
63. Fried, P.; Woodward, J.; Brown, D.; Harvell, D.; Hanken, J. 3D scanning of antique glass by combining photography and computed tomography. *Digit. Appl. Archaeol. Cult. Herit.* **2020**, *18*, e00147. [[CrossRef](#)]
64. Bertolini, M.; Rossoni, M.; Colombo, G. Operative Workflow from CT to 3D Printing of the Heart: Opportunities and Challenges. *Bioengineering* **2021**, *8*, 130. [[CrossRef](#)]
65. Byrne, N.; Velasco Forte, M.; Animesh, T.; Valverde, I.; Hussain, T. A systematic review of image segmentation methodology, used in the additive manufacture of patient-specific 3D printed models of the cardiovascular system. *JRSM Cardiovasc. Dis.* **2016**, *5*, 1–9. [[CrossRef](#)]

66. Bücking, T.M.; Hill, E.R.; Robertson, J.L.; Maneas, E.; Plumb, A.A.; Nikitichev, D.I. From medical imaging data to 3D printed anatomical models. *PLoS ONE* **2017**, *12*, e0178540. [[CrossRef](#)]
67. Osti, F.; Santi, G.M.; Neri, M.; Liverani, A.; Frizziero, L.; Stilli, S.; Maredi, E.; Zarantonello, P.; Gallone, G.; Stallone, S.; et al. CT Conversion Workflow for Intraoperative Usage of Bony Models: From DICOM Data to 3D Printed Models. *Appl. Sci.* **2019**, *9*, 708. [[CrossRef](#)]
68. Robles, M.; Carew, R.M.; Morgan, R.M.; Rando, C. A step-by-step method for producing 3D crania models from CT data. *Forensic Imaging* **2020**, *23*, 200404. [[CrossRef](#)]
69. Sainsbury, B.; Wilz, O.; Ren, J.; Green, M.; Fergie, M.; Rossa, C. Preoperative Virtual Reality Surgical Rehearsal of Renal Access during Percutaneous Nephrolithotomy: A Pilot Study. *Electronics* **2022**, *11*, 1562. [[CrossRef](#)]
70. Wake, N.; Rosenkrantz, A.; Huang, W.; Wysock, J.; Taneja, S.; Sodickson, D.; Chandarana, H. A workflow to generate patient-specific three-dimensional augmented reality models from medical imaging data and example applications in urologic oncology. *3D Print. Med.* **2021**, *7*, 34. [[CrossRef](#)] [[PubMed](#)]
71. Kamio, T.; Onda, T. Fused Deposition Modeling 3D Printing in Oral and Maxillofacial Surgery: Problems and Solutions. *Cureus* **2022**, *14*, e28906. [[CrossRef](#)] [[PubMed](#)]
72. Ravi, T.; Ranganathan, R.; Pugalandhi, A.; Arumugam, S. 3D Printed Patient Specific Models from Medical Imaging—A General Workflow. *Mater. Today Proc.* **2020**, *22*, 1237–1243. [[CrossRef](#)]
73. Otton, J.; Birbara, N.; Hussain, T.; Greil, G.; Foley, T.; Pather, N. 3D printing from cardiovascularCT: A practical guide and review. *Cardiovasc. Diagn. Ther.* **2017**, *7*, 507–526. [[CrossRef](#)]
74. Robinson, R.; Valindria, V.; Bai, W.; Oktay, O.; Kainz, B.; Suzuki, H.; Sanghvi, M.; Aung, N.; Paiva, J.; Zemrak, F.; et al. Automated Quality Control in Image Segmentation: Application to the UK Biobank Cardiac MR Imaging Study. *J. Cardiovasc. Reson.* **2019**, *21*, 18. [[CrossRef](#)]
75. Stanford Medicine. Creating STL Files for 3D Printing. 3D and Quantitive Imaging Laboratory. Department of Radiology. Available online: <https://3dqmlab.stanford.edu/creating-stl-files-for-3d-printing> (accessed on 21 June 2024).
76. Khan, U.; Yasin, A.; Abid, M.; Awan, I.S.; Khan, S.A. A Methodological Review of 3D Reconstruction Techniques in Tomographic Imaging. *J. Med. Syst.* **2018**, *42*, 190. [[CrossRef](#)]
77. RadiAnt Dicom Viewer. Available online: <https://www.radiantviewer.com/> (accessed on 21 June 2024).
78. Cignoni, P.; Callieri, M.; Corsini, M.; Dellepiane, M.; Ganovelli, F.; Ranzuglia, G. MeshLab: An Open-Source Mesh Processing Tool. In Proceedings of the European Interdisciplinary Cybersecurity Conference, Salerno, Italy, 2–4 July 2008; pp. 129–136.
79. The WebGL API—Khronos Group. Available online: <https://www.khronos.org/api/webgl> (accessed on 21 June 2024).
80. Bardis, G.; Koumpouros, Y.; Sideris, N.; Voulodimos, A.; Doulamis, N. WebGL enabled smart avatar warping for bodyweight animated evolution. *Entertain. Comput.* **2019**, *32*, 100324. [[CrossRef](#)]
81. Makris, D.; Sakellariou, C.; Karampinis, L. Emerging materiality through dynamic digital conservation. *Digit. Appl. Archaeol. Cult. Herit.* **2021**, *23*, e00198. [[CrossRef](#)]
82. Bolliger, S.; Oesterhelweg, L.; Spendlove, D.; Ross, S.N.; Thali, M. Is Differentiation of Frequently Encountered Foreign Bodies in Corpses Possible by Hounsfield Density Measurement? *J. Forensic Sci.* **2009**, *54*, 1119–1122. [[CrossRef](#)] [[PubMed](#)]
83. Choi, H.; Lee, H.J.; Kang, S.G. The Clinical Significance of Hounsfield Number of Metallic and Non-Metallic Foreign Bodies in the Soft Tissue. *Soonchunhyang Med. Sci.* **2010**, *16*, 226–230.
84. Paulis, L.E.; Kroll, J.; Heijnens, L.; Huijnen, M.; Gerretsen, R.; Backes, W.H.; Hofman, P.A.M. Is CT bulletproof? On the use of CT for characterization of bullets in forensic radiology. *Int. J. Leg. Med.* **2019**, *133*, 1869–1877. [[CrossRef](#)] [[PubMed](#)]
85. Baydoun, A.M.R.; Hamade, R.F. Differentiating and predicting HU values of 12 aluminum alloys via X-ray computed tomography. *Mater. Chem. Phys.* **2023**, *301*, 127611. [[CrossRef](#)]

Disclaimer/Publisher’s Note: The statements, opinions and data contained in all publications are solely those of the individual author(s) and contributor(s) and not of MDPI and/or the editor(s). MDPI and/or the editor(s) disclaim responsibility for any injury to people or property resulting from any ideas, methods, instructions or products referred to in the content.